RSC Advances

PAPER

View Article Online
View Journal | View Issue

Cite this: *RSC Adv.*, 2022, **12**, 28929

Nanostructured IrO_x supported on N-doped TiO_2 as an efficient electrocatalyst towards acidic oxygen evolution reaction†

Guoqiang Li, *[a] Hongrui Jia,[a] Huan Liu,[b] Xin Yang[a] and Meng-Chang Lin [a]

Received 27th August 2022
Accepted 4th October 2022

DOI: 10.1039/d2ra05374h

rsc.li/rsc-advances

Reducing the Ir consumption without compromising the catalytic performance for the oxygen evolution reaction (OER) is highly paramount to promote the extensive development of the environmentally-friendly solid polymer electrolyte water electrolysis (SPEWE) system. Herein, TiO_2 is doped with N through facile NH_3 gas treatment and innovatively employed to support IrO_x nanoparticles towards acidic OER. N-doping action not only dramatically boosts the electrical conductivity and dispersing/anchoring effects of TiO_2, but also effectively improves the electron-transfer procedure. As a result, the IrO_x/N–TiO_2 electrocatalyst exhibits prominent catalyst utilization, catalytic activity and stability. Specifically, the overpotential required to deliver 10 mA cm^{-2} is only 270 mV, and the mass activity climbs to 278.7 A g_{Ir}^{-1} @ 1.55 V_{RHE}. Moreover, the single cell voltage is only 1.761 V @ 2.0 A cm^{-2} when adopting IrO_x/N–TiO_2 as the anode catalyst, which is 44 mV lower than that of the commercial IrO_2 counterpart.

Introduction

Energy shortage and environmental issues urgently call for clean and sustainable fuels; due to the high energy density, extensive sources and environmental friendliness, hydrogen (H_2) is regarded as a promising alternative to traditional fossil fuels.[1–3] At present, H_2 is mainly generated from coal gasification and methane-steam reforming; irreconcilable conflict between the hydrogen production and environmental destruction is bound to exist.[3,4] Alternatively, photocatalytic hydrogen production is also very popular, due to the endless solar energy and environmental friendliness.[5–8] More notably, water electrolysis powered by renewable electricity is regarded as an extremely promising technique, especially the solid polymer electrolyte water electrolysis (SPEWE) with prominent advantages of high H_2 purity, high current density, low ohmic loss, compact system design and rapid system response, has attracted widespread research focus.[9–13] The oxygen evolution reaction (OER) occurring on the anode side of a water electrolyzer dominates the overall efficiency because of the sluggish kinetics.[12,14–16] At present, Ir and Ru oxides are still the most representative OER electrocatalysts, especially the Ir oxide with more prominent practical potentiality, regrettably, extremely low reserve of Ir element in the earth's crust (0.001 ppm) impedes its widespread application.[17–21] Hence, reducing the Ir consumption without compromising the OER catalytic performance is highly paramount.

Benefiting from the comprehensive support effect including effective dispersing, anchoring, electronic structure modulation and coordination, support materials have achieved widespread application in several typical electrocatalytic systems, such as the hydrogen oxidation/evolution reactions (HOR/HER),[22–26] oxygen reduction reaction/OER (ORR/OER),[27–29] CO_2 reduction reaction (CO_2RR),[30,31] N_2 reduction reaction (N_2RR),[32,33] *etc.* Among them, high anodic potential and harsh acidic circumstances make the widely used carbon-based materials unstable as the support towards acidic OER,[34,35] seeking for suitable corrosion-resistant support candidate is urgently yet highly challenging.

Up to now, acid-resistant metal compounds based on Ti and Sn elements have been widely researched and confirmed the effectiveness as support materials on catalyzing OER. It is well-known that TiO_2 and SnO_2 are semiconductors with poor electrical conductivity, active species supported on them are strictly limited to participate the reaction. There are two mainstream strategies to overcome this issue, nonstoichiometric and heteroatom-doping treatments. The electrical conductivity of TiO_2 that generally below 10^{-4} S cm^{-1} can dramatically increase to ultrahigh 10^3 S cm^{-1} of nonstoichiometric Ti_4O_7.[36–38] Gago *et al.* synthesized Ir/Ti_4O_7 catalyst with Ti_4O_7 as the support, the mass activity was as high as 4.2 A g_{Ir}^{-1} @ 1.48 V, remarkably larger than that of Ir-black (1.6 A g_{Ir}^{-1}), indicating the improved

[a]College of Energy Storage Technology, Shandong University of Science and Technology, Qingdao 266590, China. E-mail: ligq@sdust.edu.cn

[b]Qingdao Institute of Bioenergy and Bioprocess Technology, Chinese Academy of Sciences, Qingdao 266101, China

† Electronic supplementary information (ESI) available: Materials, detailed experimental section, additional experimental Figures and Tables. See https://doi.org/10.1039/d2ra05374h

Ir metal utilization.[38] Hu *et al.* applied Nb-doped TiO_2 to support IrO_2 nanoparticles, the mass activity significantly increased from 198 A $g_{IrO_2}^{-1}$ of unsupported IrO_2 to 471 A $g_{IrO_2}^{-1}$ of supported IrO_2/Nb–TiO_2 at 1.6 V, accompanied with enhanced stability.[39] For SnO_2, Sb-doped SnO_2 (ATO) is the most common improver. Böhm *et al.* prepared macroporous ATO with the electrical conductivity of 3.6 S cm^{-1}, obviously higher than that of SnO_2 (3.8×10^{-4} S cm^{-1}), the corresponding IrO_x/ATO catalyst exhibited the mass activity of 63 A g_{Ir}^{-1} @ 1.53 V and enhanced stability.[40] Similarly, Strasser *et al.* also confirmed the promoting effect of ATO support on the Ir nanodendrites.[41] Expect for the metal oxide, metal nitride such as TiN also displays promising support effect. Xing *et al.* revealed the high electrical conductivity (28.18 S cm^{-1}) of TiN, and its effectiveness of dispersing, anchoring and electronic structure modulation on IrO_2@Ir nanoparticles.[28] Afterwards, Hu *et al.* verified that TiN significantly improved the IrO_2 utilization, the mass activity climbed to 874 A $g_{IrO_2}^{-1}$ @ 1.6 V.[42]

As another style of heteroatom-doping treatment, non-metal such as N, B, F, P can also be doped into TiO_2 and generally applied in various photocatalytic systems. Saini *et al.* synthesized N–TiO_2 and B–TiO_2 through a sol–gel route and verified the effectiveness on the photocatalytic degradation of emerging micro-pollutants.[43] Xu *et al.* successfully prepared F–TiO_2, which showed enhanced photocatalytic activity for the phenol degradation.[44] Chevalier *et al.* also prepared F–TiO_2 by an emulsions method and exhibited remarkably higher efficiency for the photocatalytic degradation of nitrobenzene.[45] O'Shea *et al.* co-doped TiO_2 with N, F and P, the photocatalytic activity of this modified TiO_2 to produce hydroxyl radicals under ultra violet (UV) and visible light irradiation can be dramatically improved.[46] These cases mentioned-above mainly benefit from the decreased band-gap and the red-shift of light absorption profile to the visible region of TiO_2 through non-metal element doping.

Herein, we successfully doped TiO_2 with N element and synthesized IrO_x/N–TiO_2 electrocatalyst to catalyze OER. N-doping procedure dramatically increases the electrical conductivity of TiO_2, and subsequently improves the dispersing/stabilizing effects on IrO_x, weakens the oxidative dissolution of Ir species. Satisfactory, enhanced catalyst utilization and catalytic performance are simultaneously realized.

Results and discussion

Fig. 1a illustrates the procedure to synthesize N–TiO_2 support through NH_3 treatment and IrO_x/N–TiO_2 catalyst through ethylene glycol (EG) refluxing reduction method, respectively. Interestingly, the as-obtained N–TiO_2 appears light-blue color, apparently different from TiO_2 with pure-white, implying the band gap change due to the N-doping treatment. As shown in Fig. 1b, the common X-ray diffraction (XRD) peaks of N–TiO_2 and TiO_2 ascribe to the anatase phase of TiO_2.[47] The apparently sharper diffraction peaks of N–TiO_2 indicate the enlarged crystal size through the heating treatment. Notably in the inset of Fig. 1b, the N–TiO_2 (101) crystal diffraction facet slightly moves to a lower diffraction angle compared with TiO_2, demonstrating the successful incorporation of N into the TiO_2 lattice. Furthermore, IrO_x/N–TiO_2, IrO_x/TiO_2 and IrO_x show common crystal diffraction facets of (111), (200), (220) and (311) (Fig. 1c), ascribing to the cubic phase of Ir.[41,48] Meanwhile, diffraction peaks of anatase phase TiO_2 are also apparently recognized for the supported catalysts.

The morphology characteristics of these as-prepared samples were revealed by transmission electron microscopy (TEM). As shown in Fig. S1 (ESI†), N peak appears distinctly in the energy-dispersive X-ray spectroscopy (EDX), and the atomic/weight contents of N element are 3.60 at%/1.89 wt%, respectively, again verifies the effective doping procedure. TEM image in Fig. 1d shows the uniform dispersion of IrO_x nanoparticles on the N–TiO_2 support, while the relatively nonuniform dispersion appears when using TiO_2 support (Fig. 1f). The keys lie in the formation of Ti^{3+} species and the oxygen vacancies due to the N-doping treatment.[49,50] Ti^{3+} with reductibility can easily adsorb the $IrCl_6^{2-}$ precursor ion with high-valent Ir^{4+} species during the synthesis process, and oxygen vacancies can act as the anchoring sites for effectively adsorbing $IrCl_6^{2-}$. Therefore, improved dispersion of IrO_x on N–TiO_2 is acquired. Furthermore, unsupported IrO_x catalyst displays more noticeable particles aggregation (Fig. 1h). IrO_x/N–TiO_2 and IrO_x/TiO_2 were further characterized by the high-resolution TEM (HRTEM) (Fig. 1e and g), for the supported IrO_x nanoparticles, the interplanar spacings of 0.224 and 0.225 nm are all slightly larger than that of the standard Ir (111) crystal facet with 0.221 nm (JCPDS no. 06-0598), implying that the formation of surface oxidation state can enlarge the interplanar spacing of metallic Ir to some extent. Similarly, Luo *et al.* has reported that the interplanar spacing of Ir (111) crystal facet increased to 0.225 nm when alloyed with W metal.[51] For N–TiO_2, the interplanar spacing of 0.355 nm is slightly larger than that of the standard TiO_2 (101) crystal facet with 0.352 nm (JCPDS No. 21-1272), mainly resulted from the partly substitution of O^{2-} ion by N^{3-} ion with larger radius. By contrast, IrO_x/TiO_2 displays standard TiO_2 (101) crystal facet. Moreover, the adjacent IrO_x and N–TiO_2 (TiO_2) nanoparticles confirm the supported structure. The HAADF-STEM and corresponding elemental mapping images (Fig. S2, ESI†) of IrO_x/N–TiO_2 reveal that Ir, N, O and Ti element are uniformly distributed throughout the IrO_x/N–TiO_2 nanoparticles.

X-ray photoelectron spectroscopy (XPS) was applied to investigate the surface structure of the samples. The binding energy of all peaks has been calibrated with the C 1s orbit of 284.6 eV. XPS survey spectrum for N–TiO_2 (Fig. S3a, ESI†) depicts the typical Ti 2p, O 1s/KLL and N 1s orbits, and the atomic content of N is 3.79 at%, almost in accordance with the EDX result. After supporting IrO_x, Ir 4p/4d/4f orbits can also be clearly recognized (Fig. S3b, ESI†). The N 1s spectrum for IrO_x/N–TiO_2 was deconvoluted and obtained only one prominent peak (Fig. 2a). This peak at 396.70 eV is assigned to the substitutional N in Ti–N bonds, indicating that the N atoms enter into the TiO_2 lattice through replacing the O atoms.[52,53] Compared with IrO_x, the Ir 4f spectra for IrO_x/N–TiO_2 and IrO_x/TiO_2 all shifted negatively to lower electronic binding energy direction (Fig. 2b and S3c, ESI†), indicating the electron-

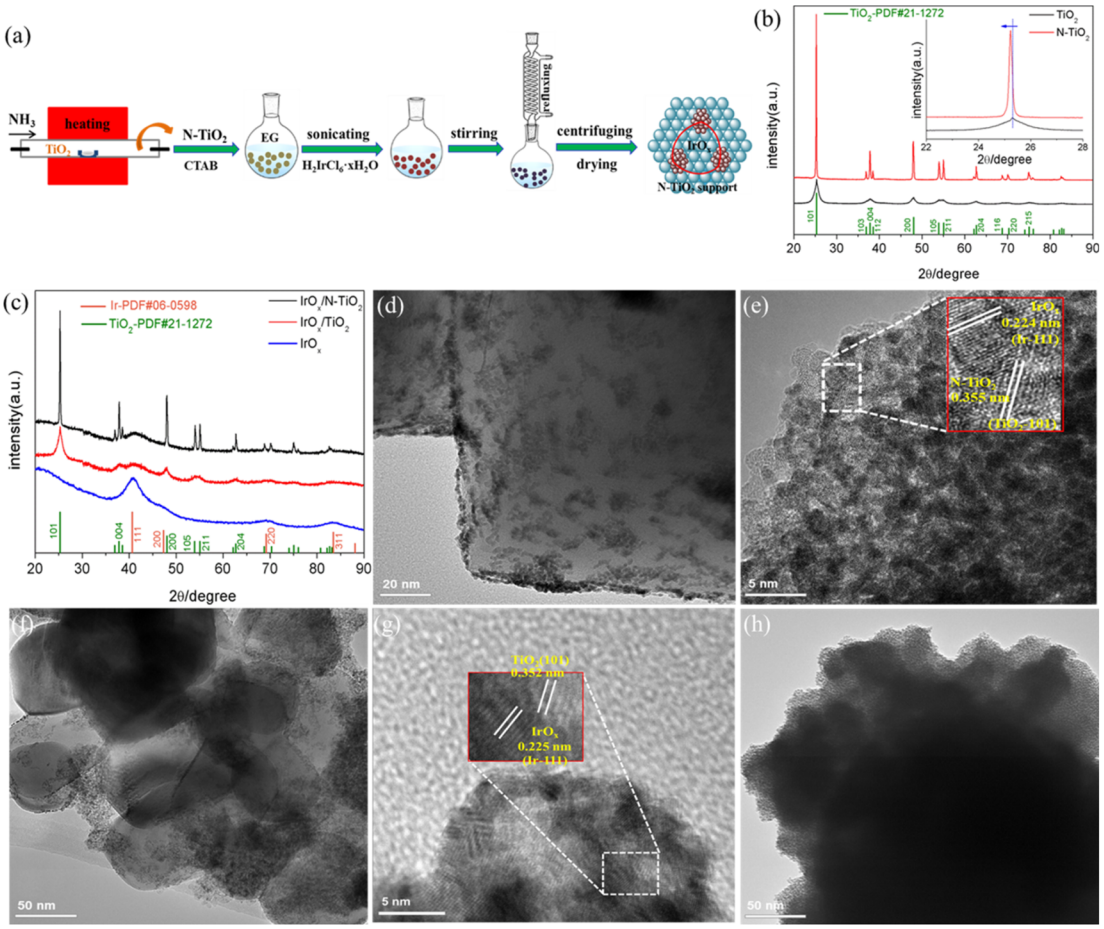

Fig. 1 (a) Synthesis route of the N–TiO_2 support and IrO_x/N–TiO_2 catalyst. XRD patterns of (b) TiO_2 and N–TiO_2 (inset: XRD patterns within 22–28°), and (c) IrO_x/N–TiO_2, IrO_x/TiO_2 and IrO_x. TEM images of (d) IrO_x/N–TiO_2, (f) IrO_x/TiO_2 and (h) IrO_x. HRTEM images of (e) IrO_x/N–TiO_2 and (g) IrO_x/TiO_2.

transfer process from N–TiO_2 and TiO_2 to IrO_x. Especially the IrO_x/N–TiO_2 with the Ir $4f_{7/2}$ orbit locates at 61.10 eV, lower by 0.16 and 0.24 eV than those of IrO_x/TiO_2 and IrO_x (Table S1, ESI†), respectively. Next, the relative contents of Ir^0 and Ir^{4+} species were obtained through deconvoluting the Ir 4f spectra, and shown in Table S1 (ESI†). For IrO_x/N–TiO_2, the content of Ir^0 species is the highest one with 66.1% (64.1% for IrO_x/TiO_2 and 63.2% for IrO_x), mainly due to the more significant electron-transfer effect. In addition, the contents of Ir^{4+} species all surpass 30%, confirming the formation of IrO_x oxide component on the catalyst surface.

The electrical conductivity of N–TiO_2 was measured to reach 0.13 S cm^{-1}, apparently higher than that of TiO_2 (7.9×10^{-6} S cm^{-1}). The significant effect of the N-doping treatment on improving the electrical conductivity of TiO_2 is undoubtable, which is beneficial for driving the supported active sites to participate the reaction. The main reason should be that strongly correlated interaction emerges between N and Ti due to the N-doping treatment, which will lead the electrons in the 3d orbit of Ti move to the 2p orbit of N. Consequently, conduction band becomes lower, band gap becomes narrower and the electrical conductivity is bound to improve.[50,54] Cyclic voltammogram (CV) tests at high scanning rate of 300 mV s^{-1} were firstly performed in N_2-saturated 0.5 M H_2SO_4 solution (Fig. 3a), subsequently, the outer charge (Q_{outer}) that assesses the accessible active surface and directly correlates with the OER activity was obtained through integrating the CV curve between 0.70 and 1.40 V.[28,55,56] As shown in the inset of Fig. 3a, the Q_{outer} of IrO_x/N–TiO_2 is 8.93 mC, about 2.83 times of IrO_x/TiO_2 (3.16 mC) and 1.28 times of IrO_x (6.97 mC), respectively. The improvement mainly resulted from the enhanced dispersing effect and electrical conductivity of the N–TiO_2 support. Furthermore, although the better dispersion of IrO_x nanoparticles on TiO_2 than the unsupported IrO_x, the ultralow electrical conductivity of TiO_2 can strictly limit the effective participation of the supported IrO_x in OER, hence, the Q_{outer} is apparently lower than that of the IrO_x catalyst. During the linear sweep voltammetry (LSV) tests (Fig. 3b), the overpotentials of the catalysts to deliver current density of 10 mA cm^{-2} follow this order: IrO_x/N–TiO_2 (270 mV) < IrO_x (286 mV) < IrO_2(CM) (307 mV) < IrO_x/TiO_2 (313 mV). Furthermore, IrO_x/N–TiO_2 shows competitively catalytic effect compared with those reported supported Ir-based

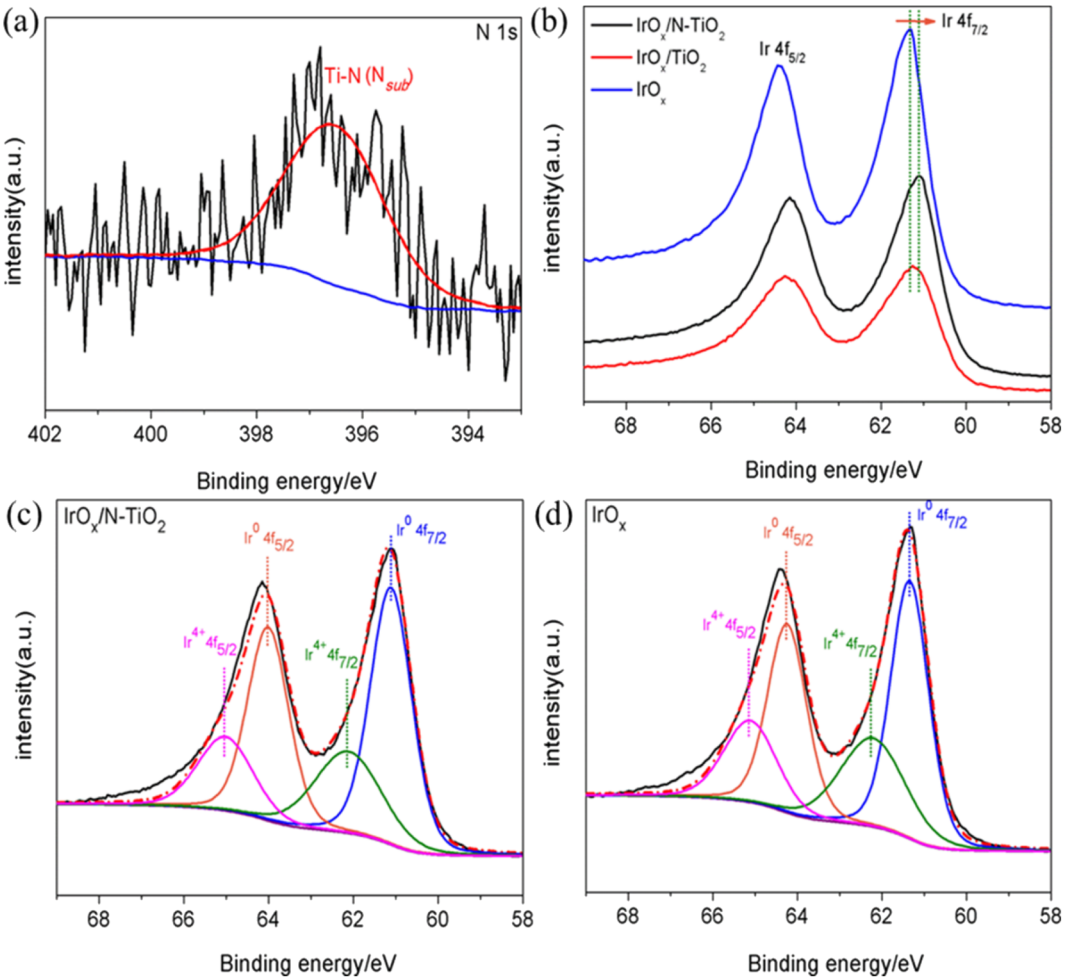

Fig. 2 (a) High-resolution XPS spectrum of the deconvoluted N 1s for $IrO_x/N–TiO_2$. (b) The comparison of the XPS spectra of Ir 4f for $IrO_x/N–TiO_2$, IrO_x/TiO_2 and IrO_x. High-resolution XPS spectra of the deconvoluted Ir 4f for (c) $IrO_x/N–TiO_2$ and (d) IrO_x.

catalysts (Table S2, ESI†). As for the pure supports, $N–TiO_2$ and TiO_2 all perform nearly negligible catalytic activity for OER, although $N–TiO_2$ performs slightly better. The corresponding mass activity curves are shown in Fig. 3c, $IrO_x/N–TiO_2$ (278.7 A g_{Ir}^{-1}) exhibits 2.70 and 2.50 times higher mass activity than those of IrO_x/TiO_2 (75.4 A g_{Ir}^{-1}) and IrO_x (79.7 A g_{Ir}^{-1}) at 1.55 V, respectively. Meanwhile, it outperforms the majority of the ever reported catalysts with similar types (Table S3, ESI†). Therefore, $N–TiO_2$ significantly improves the catalyst utilization of IrO_x for OER.

To evaluate the reaction kinetics, Tafel slopes extracted from the LSV curves were firstly investigated (Fig. 3d). $IrO_x/N–TiO_2$ possesses the smallest value of 52.2 mV dec^{-1}, indicating the most favorable OER kinetics. Subsequently, electrochemical impedance spectroscopy (EIS) tests were performed, the corresponding Nyquist plots are depicted in Fig. 3e and an equivalent circuit (EC) was adopted to fit them. As a key component, R_{ct} represents the charge transfer resistance.[57] The R_{ct} of $IrO_x/N–TiO_2$ is only 14.5 Ω, apparently smaller than those of $IrO_x/N–TiO_2$ (35.3 Ω), IrO_x (20.6 Ω) and IrO_2(CM) (35.3 Ω) (Table S4, ESI†), indicating the fastest charge transfer rate during the reaction.

Reaction stability was evaluated through galvanostatic mode, as shown in Fig. 3f, the potentials increase to varying degrees, indicating the degradation of catalytic activity. Even so, $IrO_x/N–TiO_2$ maintains favorable stability, the potential only increased by 23.8 mV after 10 h, outperforms other counterparts (39.5 mV for IrO_x/TiO_2, 60.2 mV for IrO_x, 45.7 mV for IrO_2(CM)) (Fig. 3g). Subsequently, LSV tests were applied again to investigate the maintained catalytic activity after the stability tests (Fig. S4, ESI†). $IrO_x/N–TiO_2$ still shows outstanding performance, with the potential only increased by 21.7 mV at 10 mA cm^{-2}. Inductively coupled plasma optical emission spectroscopy (ICP-OES) analysis was also carried to investigate the electrochemically dissolved Ir species (Fig. 3h). Thanks to the transferred electrons from $N–TiO_2$, the Ir mass-loss ratio of supported IrO_x is only 14.86%, by contrast, the values of IrO_x/TiO_2 and IrO_x reach as high as 25.46 and 31.65%, respectively. Hence, $N–TiO_2$ can weaken the oxidative dissolution of Ir species.

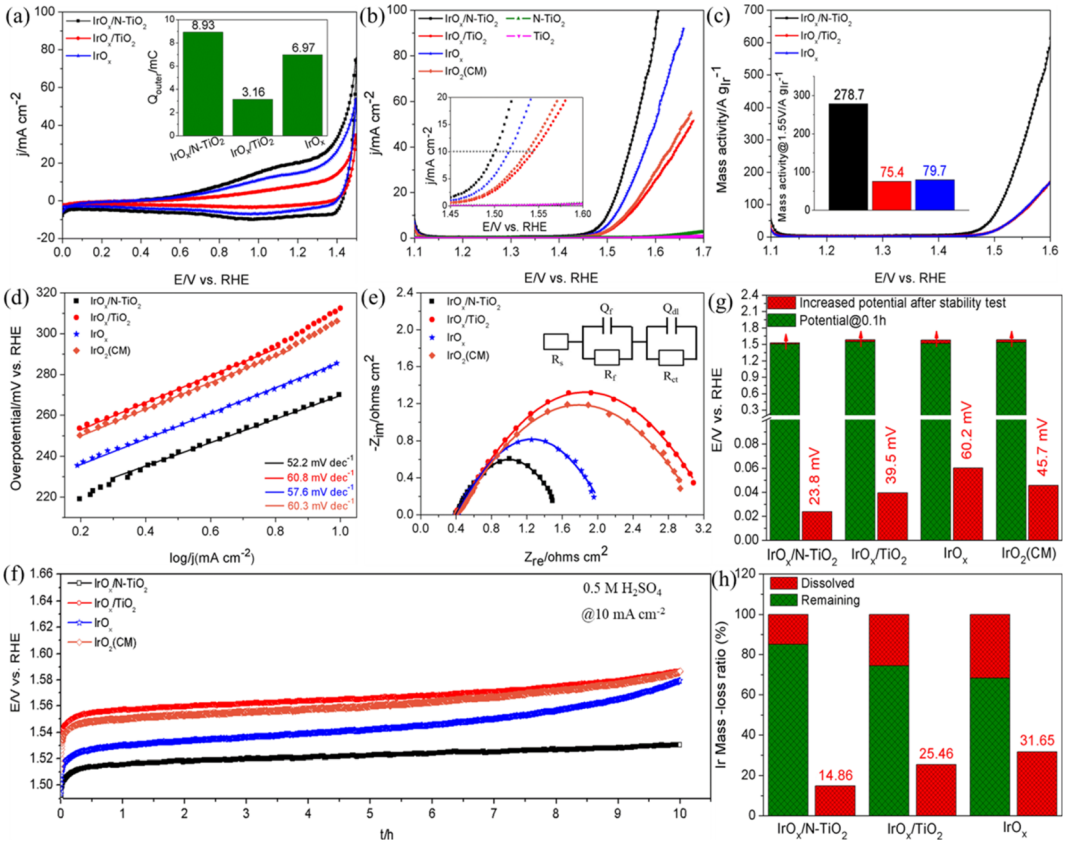

Fig. 3 (a) CV curves at the scanning rate of 300 mV s^{-1} in N_2-saturated 0.5 M H_2SO_4 solution (inset: histograms of outer charge). (b) LSV curves at the scanning rate of 5 mV s^{-1} (inset: LSV curves of the current density within 0 and 20 mA cm^{-2}). (c) Mass activity obtained from the LSV tests. (d) Tafel plots obtained from the LSV curves in (b). (e) Nyquist plots for OER at 1.55 V in a sweeping frequency range from 0.1 Hz to 10 kHz (inset: equivalent circuit). (f) Potential-time curves at the constant current density of 10 mA cm^{-2} for 10 h in N_2-saturated 0.5 M H_2SO_4 solution. (g) Histograms of the potential change. (h) Histograms of the Ir mass-loss ratio after the stability tests.

A two-electrode cell driving overall water splitting was assembled by employing IrO_x/N–TiO_2, IrO_x and IrO_2(CM) as the anode catalysts, Pt/C(CM) as the cathode catalyst. Polarization curves are shown in Fig. 4a, the IrO_x/N–TiO_2||Pt/C(CM)-based cell performs the lowest voltage of 1.785 V to deliver 100 mA cm^{-2}, meaning the total overpotential of only 555 mV. Compared with IrO_x||Pt/C(CM) and IrO_2(CM)||Pt/C(CM), 46 and 118 mV can be saved at 100 mA cm^{-2}, respectively. Furthermore, IrO_x/N–TiO_2||Pt/C(CM) exhibits favorable stability during the 20 h galvanostatic tests at constant 10 mA cm^{-2} (Fig. 4b). The structural stability was confirmed by TEM characterization and shown in Fig. 4c, well dispersion of IrO_x nanoparticles on the whole verifies the enhanced anchoring effect of N–TiO_2.

To scrutinize the practical application potential of IrO_x/N–TiO_2, proton exchange membrane water electrolysis (PEMWE) single cell was assembled with Nafion® 115 proton exchange membrane as the SPE, IrO_x/N–TiO_2 as the anode catalyst and Pt/C(CM) as the cathode catalyst. By contrast, the IrO_2(CM)||Pt/C(CM)-based cell was also assembled. For IrO_x/N–TiO_2||Pt/C(CM), the required voltages to deliver 1 and 2 A cm^{-2} are only 1.672 and 1.761 V, respectively, lower by 41|44 mV than those of IrO_2(CM)||Pt/C(CM) (Fig. 4d). Finally, long-term stability tests of IrO_x/N–TiO_2||Pt/C(CM)-based cell were performed at constant 0.5 and 2.0 A cm^{-2} for 300 h, respectively (Fig. 4e). Significant degradations at the beginning of the stability tests (0–14 h for 0.5 A cm^{-2}; 0–23.5 h for 2.0 A cm^{-2}) are observed, which could be ascribed to two main reasons, the mass transfer polarization and the modification of the oxidation state at the anode catalyst surface.[58] The overall, initial and subsequent degradation rates are calculated and shown in Fig. 4f. Apparently, the stability performance at 2.0 A cm^{-2} (overall/initial/subsequent degradation rates of 234/1570/101.6 μV h^{-1}) is inferior to that at 0.5 A cm^{-2} (overall/initial/subsequent degradation rates of 92.2/979.5/48.6 μV h^{-1}), mainly resulted from the more seriously oxidative dissolution of Ir species and the damage of other cell components under harsher environment.

However, compared with these reported PEMWE cells employing Ir-based anode catalysts,[59–65] this IrO_x/N–TiO_2||Pt/C(CM)-based cell displays relatively mediocre level for the stability performance. Therefore, systematic optimization of the cell fabrication should be the further research emphasis for enhancing the practical cell performance, especially the operating stability.

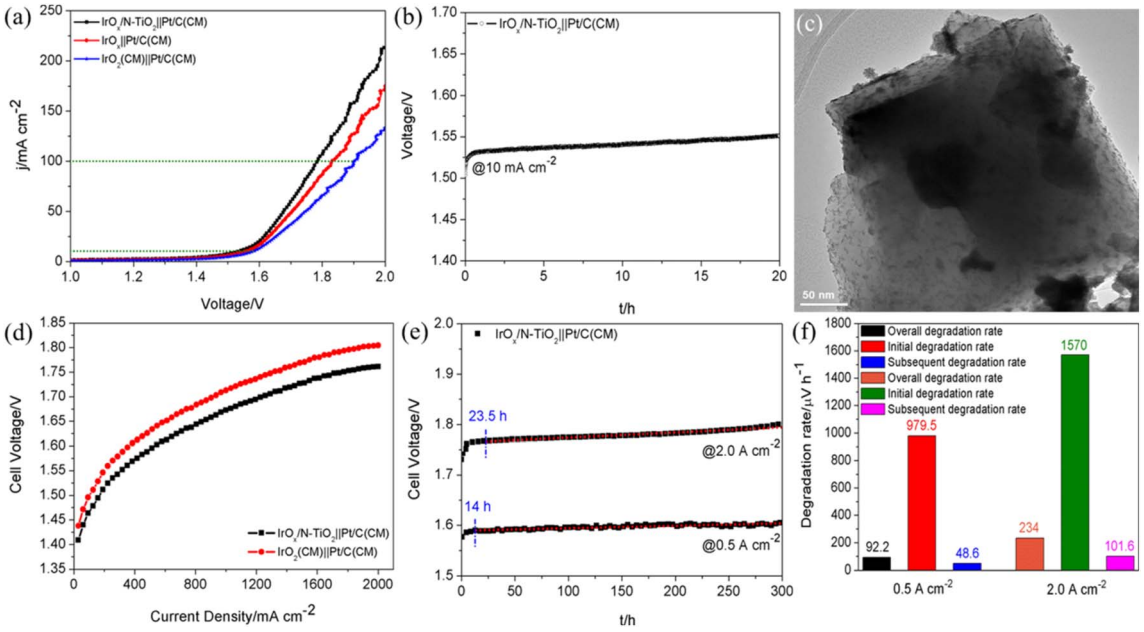

Fig. 4 (a) Polarization curves for two-electrode overall water splitting with IrO_x/N–TiO_2, IrO_x or IrO_2(CM) as the anode catalyst (loading of 0.3 mg cm^{-2}), and Pt/C(CM) as the cathode catalyst (loading of 0.1 mg cm^{-2}) at the scanning rate of 5 mV s^{-1}. (b) Voltage–time curve of IrO_x/N–TiO_2||Pt/C(CM) at the constant current density of 10 mA cm^{-2} for 20 h. (c) TEM image of IrO_x/N–TiO_2 after the stability test. (d) Steady-state polarization curves of the SPEWE single cells with IrO_x/N–TiO_2 or IrO_2(CM) as the anode catalyst (loading of 2.0 mg cm^{-2}), and Pt/C(CM) as the cathode catalyst (loading of 1.0 mg cm^{-2}). (e) Stability tests of IrO_x/N–TiO_2||Pt/C(CM)-based cell operated at the constant current densities of 0.5 and 2.0 A cm^{-2} for 300 h. The subsequent degradation rates are evaluated by means of a linear regression fit (dashed black lines). (f) Histograms of the degradation rate within the stability tests at 0.5 and 2.0 A cm^{-2}.

Conclusions

In summary, supported IrO_x/N–TiO_2 catalyst was synthesized to effectively catalyze OER. N–TiO_2 exhibits comprehensive support effect, firstly, the remarkably high electrical conductivity of 0.13 S cm^{-1} is beneficial for driving the active sites to adequately participate the reaction. Secondly, N–TiO_2 can effectively disperse and anchor the IrO_x nanoparticles. Thirdly, prominent electron-transfer from N–TiO_2 to IrO_x significantly weakens the electrochemically oxidative dissolution of Ir species. Consequently, IrO_x/N–TiO_2 performs enhanced catalytic performance, the required overpotential to drive 10 mA cm^{-2} is only 270 mV, accompanied with improved catalyst utilization, favorable reaction kinetics and enhanced stability. Moreover, the single cell employing IrO_x/N–TiO_2 performs the voltages of only 1.672 V @ 1 A cm^{-2} and 1.761 V @ 2 A cm^{-2}.

Author contributions

G. L. conceived and coordinated the research. G. L. and H. J. conducted the catalyst preparation, physical characterization and electrochemical measurement. G. L., X. Y. and M-C. L. contributed to the analysis of experiment results. The manuscript was primarily written and modified by G. L. and H. L. All authors contributed to the discussion and manuscript review.

Conflicts of interest

There are no conflicts to declare.

Acknowledgements

This work was supported by the Elite Program of Shandong University of Science and Technology (0104060540812), and the Qingdao Scientific and Technological Innovation High-Level Talents Project: Aluminum-Ion Power and Energy Storage Battery (17-2-1-1-zhc).

Notes and references

1 X. J. Zeng, D. R. Duan, X. F. Zhang, X. H. Li, K. Li, R. H. Yu and M. Moskovits, *J. Mater. Chem. C*, 2022, **10**, 4140–4147.
2 L. G. Li, P. T. Wang, Q. Shao and X. Q. Huang, *Adv. Mater.*, 2022, **33**, 2004243.
3 S. Roy, Z. H. Huang, A. Bhunia, A. Castner, A. K. Gupta, X. D. Zou and S. Ott, *J. Am. Chem. Soc.*, 2019, **141**, 15942–15950.
4 X. X. Zou and Y. Zhang, *Chem. Soc. Rev.*, 2015, **44**, 5148–5180.
5 G. F. Liao, C. X. Li, X. Z. Li and B. Z. Fang, *Cell Rep. Phys. Sci.*, 2021, **2**, 100355.
6 G. F. Liao, C. X. Li, S.-Y. Liu, B. Z. Fang and H. M. Yang, *Phys. Rep.*, 2022, **983**, 1–41.
7 G. F. Liao, C. X. Li, S.-Y. Liu, B. Z. Fang and H. M. Yang, *Trends Chem.*, 2022, **4**, 111–127.
8 G. F. Liao, X. Y. Tao and B. Z. Fang, *Matter*, 2022, **5**, 377–379.
9 Z. W. Lei, T. Y. Wang, B. T. Zhao, W. B. Cai, Y. Liu, S. H. Jiao, Q. Li, R. G. Cao and M. L. Liu, *Adv. Energy Mater.*, 2020, **10**, 2000478.

10 B. H. Zhou, R. J. Gao, J.-J. Zou and H. M. Yang, *Small*, 2022, **18**, 2202336.
11 S. D. Ghadge, P. P. Patel, M. K. Datta, O. I. Velikohatnyi, R. Kuruba, P. M. Shanthi and P. N. Kumta, *RSC Adv.*, 2017, **10**, 17311–17324.
12 Y. Z. Wen, P. N. Chen, L. Wang, S. Y. Li, Z. Y. Wang, J. Abed, X. N. Mao, Y. M. Min, C. D. Dinh, P. D. Luna, R. Huang, L. S. Zhang, J. Wang, L. P. Wang, R. J. Nielsen, H. H. Li, T. T. Zhuang, C. C. Ke, O. Voznyy, Y. F. Hu, Y. Y. Li, W. A. Goddard III, B. Zhang, H. S. Peng and E. H. Sargent, *J. Am. Chem. Soc.*, 2021, **143**, 6482–6490.
13 L. An, C. Wei, M. Lu, H. W. Liu, Y. B. Chen, G. G. Scherer, A. C. Fisher, P. X. Xi, Z. J. Xu and C. H. Yan, *Adv. Mater.*, 2021, **33**, 2006328.
14 Y. H. Zhao, M. H. Xi, Y. B. Qi, X. D. Sheng, P. F. Tian, Y. H. Zhu, X. L. Yang, C. Z. Li and H. L. Jiang, *J. Energy Chem.*, 2022, **69**, 330–337.
15 C. J. Liu, B. B. Sheng, Q. Zhou, D. F. Cao, H. H. Ding, S. M. Chen, P. J. Zhang, Y. J. Xia, X. J. Wu and L. Song, *Nano Res.*, 2022, **15**, 7008–7015.
16 Y. P. Liu, X. Liang, H. Chen, R. Q. Gao, L. Shi, L. Yang and X. X. Zou, *Chin. J. Catal.*, 2021, **42**, 1054–1077.
17 Z. J. Chen, X. G. Duan, W. Wei, S. B. Wang and B.-J. Ni, *Nano Energy*, 2020, **78**, 105392.
18 Z. L. Fan, Y. J. Ji, Q. Shao, S. Z. Geng, W. X. Zhu, Y. Liu, F. Liao, Z. W. Hu, Y.-C. Chang, C.-W. Pao, Y. Y. Li, Z. H. Kang and M. W. Shao, *Joule*, 2021, **5**, 3221–3234.
19 Y. B. Wang, S. Hou, R. P. Ma, J. D. Jiang, Z. P. Shi, C. P. Liu, J. J. Ge and W. Xing, *ACS Sustainable Chem. Eng.*, 2021, **9**, 10710–10716.
20 H. Chen, L. Shi, X. Liang, L. N. Wang, T. Asefa and X. X. Zou, *Angew. Chem., Int. Ed.*, 2020, **59**, 19654–19658.
21 L. F. Lu, H. Zheng, Y. X. Li, Y. H. Zhou and B. Z. Fang, *Chem. Eng. J.*, 2023, **451**, 138668.
22 G. H. Bae, D. H. Youn, S. Han and J. S. Lee, *Carbon*, 2013, **51**, 274–281.
23 M. K. Kundu, T. Bhowmik, R. Mishra and S. Barman, *ChemSusChem*, 2018, **11**, 2388–2401.
24 Y. H. Liu, Q. L. Wang, J. C. Zhang, J. Ding, Y. Q. Cheng, T. Wang, J. Li, F. X. Hu, H. B. Yang and B. Liu, *Adv. Energy Mater.*, 2022, **12**, 2200928.
25 Q. Yang, H. X. Liu, P. Yuan, Y. Jia, L. Z. Zhuang, H. W. Zhang, X. C. Yan, G. H. Liu, Y. F. Zhao, J. Z. Liu, S. Q. Wei, L. Song, Q. L. Wu, B. Q. Ge, L. Z. Zhang, K. Wang, X. Wang, C.-R. Chang and X. D. Yao, *J. Am. Chem. Soc.*, 2022, **144**, 2171–2178.
26 L. F. Lu, S. H. Zou and B. Z. Fang, *ACS Catal.*, 2021, **11**, 6020–6058.
27 J. Liu, M. G. Jiao, B. B. Mei, Y. X. Tong, Y. P. Li, M. B. Ruan, P. Song, G. Q. Sun, L. H. Jiang, Y. Wang, Z. Jiang, L. Gu, Z. Zhou and W. L. Xu, *Angew. Chem., Int. Ed.*, 2019, **58**, 1163–1167.
28 G. Q. Li, K. Li, L. Yang, J. F. Chang, R. P. Ma, Z. J. Wu, J. J. Ge, C. P. Liu and W. Xing, *ACS Appl. Mater. Interfaces*, 2018, **10**, 38117–38124.
29 X. Z. Zheng, M. K. Qin, S. X. Ma, Y. Z. Chen, H. H. Ning, R. Yang, S. J. Mao and Y. Wang, *Adv. Sci.*, 2022, **9**, 2104636.
30 C. Lim, W. H. Lee, J. H. Won, Y.-J. Ko, S. Kim, B. K. Min, K.-Y. Lee, W. S. Jung and H.-S. Oh, *Adv. Sustainable Syst.*, 2022, **6**, 2200019.
31 B. H. Zhang, Y. Z. Jiang, M. X. Gao, T. Y. Ma, W. P. Sun and H. G. Pan, *Nano Energy*, 2021, **80**, 105504.
32 M. L. Yuan, H. H. Zhang, D. L. Gao, H. Y. He, Y. Sun, P. L. Hu, S. Dipazir, Q. G. Li, L. Zhou, S. W. Li, Z. J. Liu, J. H. Yang, Y. B. Xie, H. Zhao and G. J. Zhang, *J. Mater. Chem. A*, 2020, **8**, 2691–2700.
33 L. Shi, S. N. Bi, Y. Qi, R. F. He, K. Ren, L. R. Zheng, J. O. Wang, G. L. Ning and J. W. Ye, *ACS Catal.*, 2022, **12**, 7655–7663.
34 G. C. da Silva, S. I. Venturini, S. Y. Zhang, M. Löffler, C. Scheu, K. J. J. Mayrhofer, E. A. Ticianelli and S. Cherevko, *ChemElectroChem*, 2020, **7**, 2330–2339.
35 C. Spöri, J. T. H. Kwan, A. Bonakdarpour, D. P. Wilkinson and P. Strasser, *Angew. Chem., Int. Ed.*, 2017, **56**, 5994–6021.
36 S. H. Yang, Y. Li, J. Sun and B. Q. Cao, *J. Power Sources*, 2019, **431**, 220–225.
37 F. C. Walsh and R. G. A. Wills, *Electrochim. Acta*, 2010, **55**, 6342–6351.
38 L. Wang, P. Lettenmeier, U. Golla-Schindler, P. Gazdzicki, N. A. Cañas, T. Morawietz, R. Hiesgen, S. S. Hosseiny, A. S. Gago and K. A. Friedrich, *Phys. Chem. Chem. Phys.*, 2016, **18**, 4487–4495.
39 W. Hu, S. L. Chen and Q. H. Xia, *Int. J. Hydrogen Energy*, 2014, **39**, 6967–6976.
40 D. Böhm, M. Beetz, M. Schuster, K. Peters, A. G. Hufnagel, M. Döblinger, B. Böller, T. Bein and D. Fattakhova-Rohlfing, *Adv. Funct. Mater.*, 2019, **30**, 1906670.
41 H.-S. Oh, H. N. Nong, T. Reier, M. Gliech and P. Strasser, *Chem. Sci.*, 2015, **6**, 3321–3328.
42 K. K. Zhang, W. S. Mai, J. Li, H. Wang, G. Q. Li and W. Hu, *J. Mater. Sci.*, 2020, **55**, 3507–3520.
43 V. Yadav, H. Sharma, A. Rana and V. K. Saini, *J. Ind. Eng. Chem.*, 2022, **107**, 126–136.
44 Y. J. Gao and Y. M. Xu, *Acta Phys.-Chim. Sin.*, 2012, **28**, 641–646.
45 N. Fessi, M. F. Nsib, Y. Chevalier, C. Guillard, F. Dappozze, A. Houas, L. Palmisano and F. Parrino, *Langmuir*, 2020, **36**, 13545–13554.
46 A. M. Abdullah, M. Á. Gracia-Pinilla, S. C. Pillai and K. O'Shea, *Molecules*, 2019, **24**, 2147.
47 H. J. Chen, G. R. Deng, Z. S. Feng, Z. Q. Xu, M. Y. Yang, Y. Huang, Q. L. Peng, T. S. Li and Y. Wang, *Chem. Commun.*, 2022, **58**, 3214–3217.
48 L. H. Zu, X. Y. Qian, S. L. Zhao, Q. H. Liang, Y. E. Chem, M. Liu, B.-J. Su, K.-H. Wu, L. B. Qu, L. L. Duan, H. L. Zhan, J.-Y. Zhang, C. Li, W. Li, J. Y. Juang, J. W. Zhu, D. Li, A. B. Yu and D. Y. Zhao, *J. Am. Chem. Soc.*, 2022, **144**, 2208–2217.
49 S. Khan, T. L. Ruwer, N. Khan, A. Köche, R. W. Lodge, H. Coelho-Júnior, R. L. Sommer, M. J. L. Santos, C. F. Malfatti, C. P. Bergmann and J. A. Fernandes, *J. Mater. Chem. A*, 2021, **9**, 12214–12224.
50 M. N. Fan, Z. H. Lin, P. Zhang, X. D. Ma, K. P. Wu, M. L. Liu and X. H. Xiong, *Adv. Energy Mater.*, 2021, **11**, 2003037.

51 L. H. Fu, X. Hu, Y. B. Li, G. Z. Cheng and W. Luo, *Nanoscale*, 2019, **11**, 8898–8905.
52 Q. Q. Chen, A. Ozkan, B. Chattopadhyay, K. Baert, C. Poleunis, A. Tromont, R. Snyders, A. Delcorte, H. Terryn, M. P. Delplancke-Ogletree, Y. H. Geerts and F. Reniers, *Langmuir*, 2019, **35**, 7161–7168.
53 Y. Wang, C. X. Feng, M. Zhang, J. J. Yang and Z. J. Zhang, *Appl. Catal., B*, 2010, **100**, 84–90.
54 L. Xu, C. Q. Tang, L. Dai, D. H. Tang and X. G. Ma, *Acta Phys. Sin.*, 2007, **56**, 1048–1053.
55 G. F. Li, H. M. Yu, X. Y. Wang, D. L. Yang, Y. K. Li, Z. G. Shao and B. L. Yi, *J. Power Sources*, 2014, **249**, 175–184.
56 W. Hu, Y. Q. Wang, X. H. Hu, Y. Q. Zhou and S. L. Chen, *J. Mater. Chem.*, 2012, **22**, 6010–6016.
57 R. P. Ma, Y. Wang, G. Q. Li, L. Yang, S. W. Liu, Z. Jin, X. Zhao, J. J. Ge and W. Xing, *Nano Res.*, 2021, **14**, 4321–4327.
58 S. Siracusano, S. Trocino, N. Briguglio, F. Pantò and A. S. Aricò, *J. Power Sources*, 2020, **468**, 228390.
59 G. F. Li, H. M. Yu, W. Song, X. Y. Wang, Y. K. Li, Z. G. Shao and B. L. Yi, *Int. J. Hydrogen Energy*, 2012, **37**, 16786–16794.
60 J. B. Cheng, H. M. Zhang, G. B. Chen and Y. N. Zhang, *Electrochim. Acta*, 2009, **54**, 6250–6256.
61 K. A. Lewinski, D. F. van der Vliet and S. M. Luopa, *ECS Trans.*, 2015, **69**, 893–917.
62 M. Möckl, M. F. Ernst, M. Kornherr, F. Allebrod, M. Bernt, J. Byrknes, C. Eickes, C. Gebauer, A. Moskovtseva and H. A. Gasteiger, *J. Electrochem. Soc.*, 2022, **169**, 064505.
63 S. C. Sun, Z. G. Shao, H. M. Yu, G. F. Li and B. L. Yi, *J. Power Sources*, 2014, **267**, 515–520.
64 G. F. Li, H. M. Yu, X. Y. Wang, S. C. Sun, Y. K. Li, Z. G. Shao and B. L. Yi, *Phys. Chem. Chem. Phys.*, 2013, **15**, 2858–2866.
65 C. Rakousky, U. Reimer, K. Wippermann, S. Kuhri, M. Carmo, W. Lueke and D. Stolten, *J. Power Sources*, 2017, **342**, 38–47.